Rapid X-ray Micro-CT Imaging of Brine Imbibition in Porous Media with a Benchtop System Using Deep Learning

Ahmed Adila[1], *Kunning* Tang[1], *Peyman* Mostaghimi[1], and *Ryan* T. Armstrong[1*]

[1]School of Civil and Environmental Engineering, The University of New South Wales, Sydney, NSW, Australia

Abstract. Capturing multiphase flow in porous media at the pore scale requires high temporal resolution imaging, as fluid displacement involves rapid, transient changes in interface configuration and phase connectivity. Achieving such resolution using benchtop micro-CT systems is challenging because ultra-fast scanning reduces photon counts, resulting in high noise, motion artifacts, and low contrast between phases. Consequently, benchtop studies have been largely limited to quasi-static or low temporal resolution imaging, while synchrotron-based approaches, though capable of high-speed imaging, remain constrained by limited accessibility and experimental flexibility. In this study, we demonstrate second-scale 4D micro-CT imaging of brine imbibition in sandstone using a laboratory benchtop system, enabled by deep learning-based enhancement. Brine (30% KI) was injected at 1.2 μL/min under confining pressure conditions, and full 3D scans were acquired every 2.8 seconds at a voxel size of 15 μm. Ultra-fast reconstructions were enhanced using a cascading P3T-Net workflow trained across 1R, 8R, and high-quality image domains, enabling improved phase contrast and subsequent segmentation. The proposed approach enables quantitative, time-resolved imaging at rates far exceeding conventional benchtop systems, allowing direct observation of transient pore-scale displacement processes.

1 Introduction

Multiphase flow in porous media is fundamental to a wide range of subsurface processes, including hydrocarbon recovery, CO_2 sequestration, underground hydrogen storage, groundwater flow, and contaminant transport [1–3]. Macroscopic flow behavior in Earth science systems, such as fluid transport and trapping efficiency, typically evolves at relatively slow rates, often on the order of meters per day or lower, whereas the governing processes at the pore scale occur much more rapidly, spanning timescales from milliseconds to seconds [4,5]. At the micrometre scale, flow is dominated by capillary forces under low injection rates, where fluid displacement occurs through a sequence of pore-scale events during drainage and imbibition [6–8]. These displacement mechanisms include complex phenomena such as pore filling [9,10], snap-off [11], connectivity [12], desaturation [13], hysteresis [14], and interfacial relaxation[15], all of which strongly influence macroscopic flow behaviour. Understanding these pore-scale mechanisms is essential for improving predictions of multiphase flow in subsurface systems. For instance, in geological storage applications, such as CO_2 or hydrogen storage, the efficiency and security of storage depend on the ability of the porous medium to trap fluids within its pore network.

X-ray micro-computed tomography (micro-CT) has become a powerful non-destructive imaging technique for visualizing the internal structure of porous media and fluid distributions in three dimensions [16–18]. The quality of micro-CT images depends on factors such as contrast, spatial resolution, noise, and reconstruction artefacts, which directly affect the reliability of pore-scale analysis [19]. In conventional polychromatic micro-CT systems, the low photon flux requires long acquisition times, requiring the sample to remain static for extended periods ranging from minutes to hours [20]. As a result, fluid displacement experiments must often be paused to allow transient flow to cease before imaging, preventing the capture of dynamic pore-scale processes.

To overcome these limitations, synchrotron-based X-ray micro-CT has been widely used due to its extremely high photon flux, which is many orders of magnitude greater than that of laboratory systems and enables sub-minute or even second temporal resolution imaging [21–24]. This capability has enabled detailed investigation of dynamic pore-scale phenomena such as capillary rise, snap-off events, ganglion dynamics, and Haines jumps [5,11,25–27]. In addition, dynamic or time-resolved "4D" micro-CT imaging has extended conventional 3D imaging by capturing temporal evolution, allowing fluid configurations and their dynamics to be monitored directly at the pore scale [20]. Several studies have successfully utilized synchrotron imaging to observe and classify real-time multiphase flow dynamics and pore-filling events [5,11,13,14,26,28–33]. However, access to synchrotron facilities remains limited and costly, restricting their routine use, and these systems may also have constraints such as limited field of view [21].

Although synchrotron imaging provides excellent temporal resolution, there is increasing demand for laboratory-based micro-CT systems that can perform dynamic imaging under more accessible conditions. Significant progress has been made in developing fast laboratory micro-CT techniques that achieve temporal resolutions on

* Corresponding author: ryan.armstrong@unsw.edu.au

the order of seconds to tens of seconds [4,16,20,34–38]. Additionally, various studies have explored hardware and software modifications to improve the temporal resolution of laboratory-based scanners. However, a fundamental trade-off remains, i.e., faster scans improve temporal resolution but introduce increased noise and artefacts due to limited angular sampling, whereas slower scans yield higher image quality but fail to capture transient pore-scale events, thereby limiting accurate interpretation of dynamic processes [4,16,20,39].

Figure 1, adapted form [16], illustrates the trade-off between spatial and temporal resolution achieved by synchrotron and laboratory-based X-ray computed tomography systems for dynamic imaging of multiphase flow in porous media. The figure summarizes the acquisition capabilities reported across a range of imaging platforms, highlighting the challenge of simultaneously achieving high spatial resolution and rapid scan times. Additional points corresponding to the CoreTom system used in this work, typical CoreTom-based porous media studies, the present ultra-fast CoreTom experiment, the deep-learning-enhanced CoreTom workflow (P3T-Net), and the Australian Nuclear Science and Technology Organization (ANSTO) MCT beamline are included for comparison.

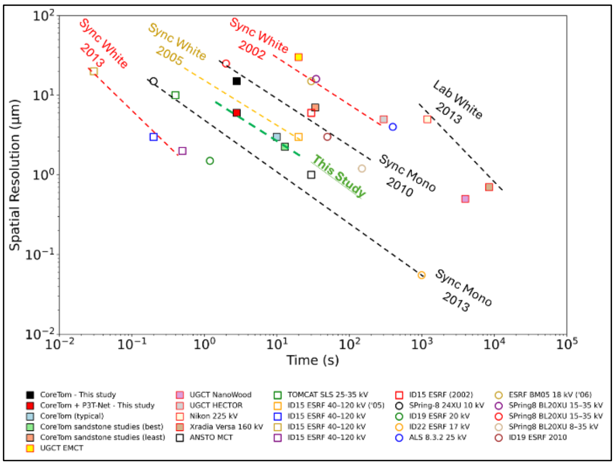

Fig. 1. Adapted from [16]: Spatial and temporal resolutions reported for synchrotron and laboratory-based X-ray computed tomography systems used for dynamic imaging of porous media. Open symbols denote synchrotron sources and filled symbols denote laboratory-based systems. Squares represent polychromatic ("white") beam configurations, while circles represent monochromatic beam configurations.

To address these challenges related to the trade-off between spatial and temporal resolution, image denoising techniques have been widely explored. Recent advances in artificial intelligence and machine learning have enabled the application of deep learning models such as convolutional neural networks, autoencoders, generative adversarial networks, and diffusion models for improving image quality and reducing noise [40–48]. Deep learning approaches have demonstrated strong capability in enhancing digital rock images through denoising, deblurring, and super-resolution, thereby improving the reliability of pore-scale analysis [49].

Despite these advancements, a significant gap remains in achieving high-quality, time-resolved imaging of multiphase flow using laboratory-based micro-CT systems, where the trade-off between temporal resolution and image reliability continues to limit accurate characterization of fast pore-scale dynamics. Moreover, there remains a lack of methods that enable quantitative, time-resolved (4D) pore-scale imaging at second-scale temporal resolution using widely accessible benchtop micro-CT systems. Addressing this limitation is essential for advancing the understanding of transient multiphase flow processes and enabling broader experimental investigations beyond specialized facilities.

To address this challenge, this study presents an approach for ultrafast 4D imaging of multiphase flow in porous media using a benchtop X-ray micro-CT system. The proposed method achieves a temporal resolution of approximately 2.8 seconds per scan, representing a substantial improvement over most laboratory-based studies, where temporal resolutions are typically on the order of tens of seconds with highly specialised hardware [33], thereby limiting the ability to resolve rapid pore-scale displacement events. To overcome the limitations associated with fast acquisitions, a deep learning-based enhancement technique is employed to improve image quality and enable quantitative analysis. As such, this work contributes toward bridging the gap between high-temporal-resolution synchrotron imaging and more accessible laboratory-based systems.

2 Materials and Methods

Pore-scale imaging experiments were conducted to investigate dynamic brine imbibition in porous media using a laboratory-based X-ray micro-computed tomography (micro-CT) system. The experimental workflow combined controlled fluid injection and ultra-fast tomographic imaging to acquire time-resolved (4D) datasets of multiphase flow. To address the reduced image quality associated with rapid acquisition, a deep learning-based enhancement approach was applied in post-processing. Multiple datasets with varying acquisition conditions were obtained, including high-quality static scans of the dry sample (3 μm voxel size) and dynamic scans reconstructed using different numbers of rotations (1, 4, and 8 rotations), enabling systematic evaluation of image quality and enhancement performance.

2.1 Samples and Fluids

A cylindrical Bentheimer sandstone core was used as the porous medium, with a diameter of 5 mm, a length of 10 mm, and a porosity of approximately 25%. The sample was initially dry, with air occupying the pore space prior to fluid injection.

The wetting phase consisted of a potassium iodide (KI) brine solution (30 wt%), selected to enhance X-ray attenuation contrast between the fluid phases. Brine was injected from the bottom of the sample at a constant flow rate of 1.2 μL/min, resulting in an imbibition process in which the wetting phase displaced the air phase. The injection continued for approximately 20 minutes, reaching a water saturation of about 60%. The injection conditions correspond to a capillary number on the order of 10^{-8}, indicating a strongly capillary-dominated flow regime, where pore-scale displacement mechanisms such as snap-off and pore-filling govern fluid redistribution.

The sample was mounted in a carbon fiber core holder (RS Systems) to ensure high X-ray transparency (Fig. 2). A confining pressure of 70 psi was applied to maintain mechanical stability and prevent bypass flow along the sample boundaries. Two Nanomite syringe pumps (Harvard apparatus) were used to control fluid injection during the experiment. The pumps were mounted directly on the micro-CT rotation stage, allowing them to rotate synchronously with the sample during continuous scanning. Electrical power was supplied via a slip-ring system integrated into the stage, enabling uninterrupted pump operation throughout the scan. The pump controllers were located outside the scanner enclosure and connected to the rotating pumps, allowing precise and stable control of the injection rate. The injection was maintained at a constant flow rate throughout the experiment, and the experiment was conducted under ambient temperature, with a confining pressure of 70 psi applied to maintain sample stability.

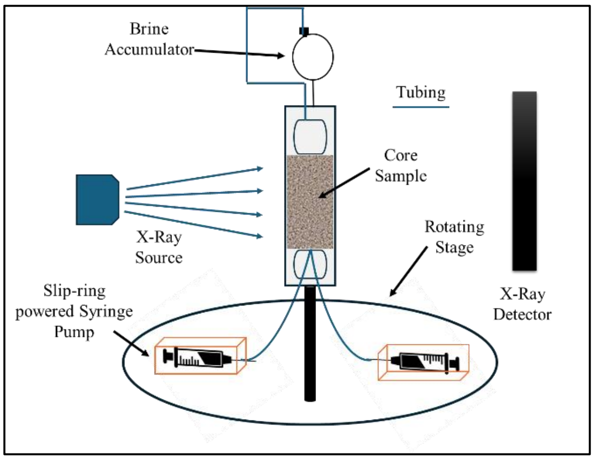

(a)

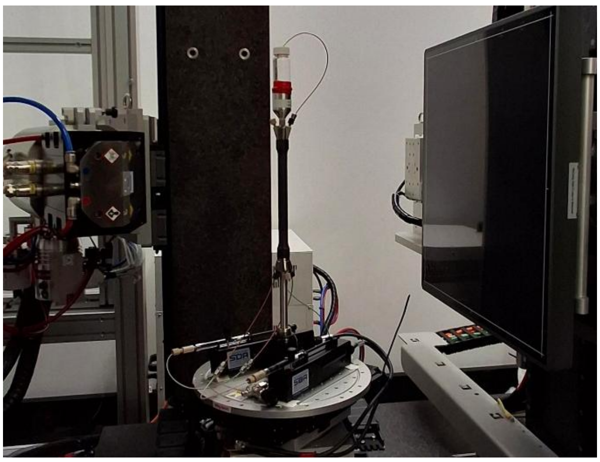

(b)

Fig. 2. Experimental set-up for dynamic micro-CT imaging.

2.2 Imaging Protocol

Dynamic imaging was performed using a CoreTOM laboratory-based micro-CT scanner (UNSW Tyree X-ray Facility). The system was operated with a microfocus X-ray source at an accelerating voltage of 140 kV and a tube power of 30 W. Projection data were acquired using a continuous rotation (dynamic) scanning mode, enabling time-resolved reconstruction of 3D volumes at a temporal resolution of approximately 2.8 seconds per scan.

Time-resolved volumes were reconstructed from subsets of continuously acquired projections. During 4D X-ray imaging, a sequence of 2D projections is recorded as the sample rotates, and each 3D volume is reconstructed from a selected group of these projections (Fig. 3a). To evaluate the trade-off between temporal resolution and image quality, reconstructions were generated using projections spanning one, four, or eight full rotations, referred to as 1R, 4R, and 8R, respectively. The 1R reconstruction provides the highest temporal resolution because it represents the shortest acquisition interval (Fig. 3b), but suffers from increased noise, poorer angular sampling, and reconstruction artefacts due to the limited number of projections and detected photons. In contrast, the 4R and 8R reconstructions combine projections from multiple rotations, improving signal quality and phase contrast at the expense of temporal resolution by averaging fluid configurations over longer time windows (Figs. 3b, c).

A total of 248,751 projections were acquired with an exposure time of approximately 14.5 ms per projection. Detector binning (factor of 3) was applied to increase acquisition speed, resulting in a voxel size of approximately 15 µm.

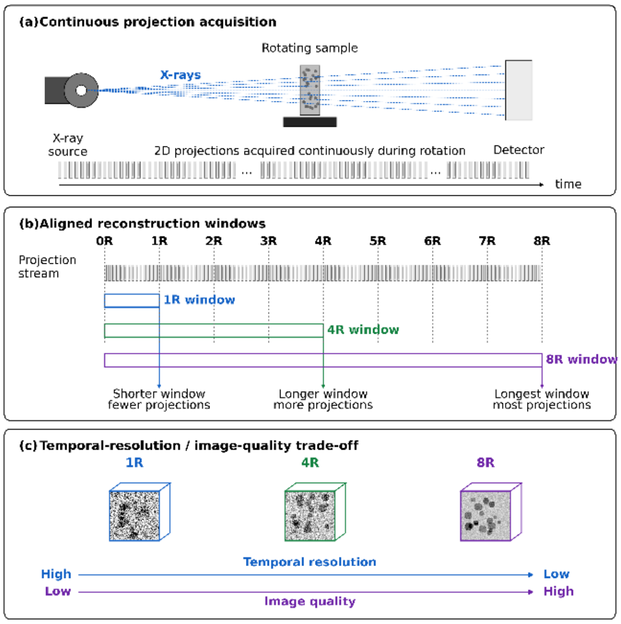

Fig. 3. Temporal resolution comparison of 1R, 4R, and 8R reconstructions from continuous projection acquisition.

2.3 Deep Learning Image Enhancement and Segmentation

To mitigate the limitations associated with fast acquisitions, a deep learning-based image enhancement approach was employed. A P3T-Net convolutional neural network was trained using paired datasets consisting of high-quality static scans (dry state) and corresponding low-quality ultra-fast dynamic scans (Fig. 4). The model was designed to suppress noise, enhance phase contrast, and preserve structural features critical for pore-scale analysis.

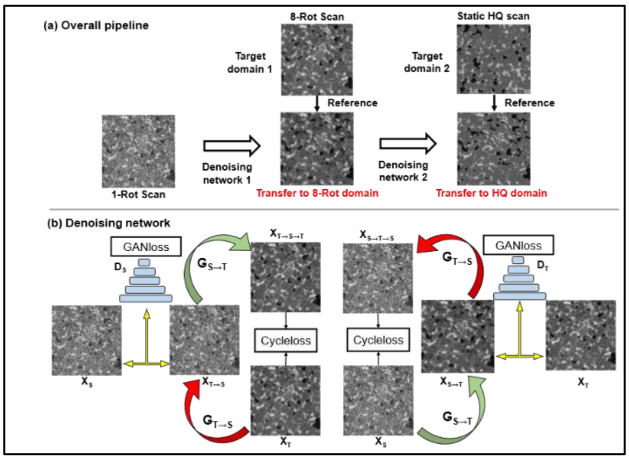

Fig. 4. Deep Learning Network Diagram.

The cascading DL-based denoising protocol is built based on the domain transfer network, P3T-Net [50]. P3T-Net is designed for unpaired scalable 3D domain transfer by combining three sequential 2D networks rather than directly processing the full 3D volume. The network first transfers source-domain 2D slices into the target-domain image style, then stacks the transferred slices into a 3D volume and applies an orthogonal-plane correction to reduce third-axis misalignment. This pseudo-3D strategy improves the applicability of 2D networks to large 3D datasets while maintaining inter-slice consistency and GPU efficiency.

In this study, two P3T-Nets were used to form a cascading denoising process. A direct single-stage transfer from the 1R scans to the high-quality (HQ) reference scans was not adopted because the domain gap between these datasets is substantial. The 1R images contain significantly higher noise levels, lower contrast, and reduced feature reliability compared with the HQ scans, making direct domain translation difficult and potentially unstable. The cascading framework addresses this challenge by progressively reducing the domain discrepancy through an intermediate 8R domain. This stepwise transfer enables more stable feature learning and improves the preservation of pore-scale structures by decomposing a complex mapping task into two simpler domain-transfer stages. The first P3T-Net uses the 1R scan as the source domain and the 8R scan as the target domain, transferring the 1R scan into the 8R domain. The second P3T-Net uses the 8R scan as the source domain and the static HQ scan as the target domain, transferring the 8R scan into the HQ domain, as shown in Figure 4a.

The domain transfer P3T-Net is constructed based on the original CycleGAN, comprising two generators ($G_{S\rightarrow T}$ and $G_{T\rightarrow S}$) and two discriminators (D_S and D_T) (as shown in Figure 4b. Generator is built on a ResNet architecture and discriminator consists of four convolutional blocks, followed by a convolutional layer that reduces the feature channels to 1, and an average pooling layer with flattening. The $G_{S\rightarrow T}$ and D_S constitute the cycle of domain transfer from the source domain to the target domain and back to the source domain. The $G_{T\rightarrow S}$ and D_T form the cycle of domain transfer from target to source and back to target. To learn the mapping between the source and target domains, adversarial loss is used, expressed as:

$$L_{GAN\,(G_{S\rightarrow T},\,D_T)} = E_{X_T\sim P_{data}(X_T)}[\log D_T(X_T)] + E_{X_S\sim P_{data}(X_S)}[\log(1 - D_T(G_{S\rightarrow T}(X_S)))] \quad (1)$$

where X_S and X_T denote samples from the source domain and target domain. In practice, the expectations in Eq. (1) are estimated by averaging over mini batches of target and domain transferred samples. The adversarial training objective is then formulated as the following min-max optimization problem:

$$G^*_{S\rightarrow T}, D^*_T = \arg\min_{G_{S\rightarrow T}} \max_{D_T} L_{GAN\,(G_{S\rightarrow T},\,D_T)} \quad (2)$$

Similar adversarial loss is formulated for the transfer from target domain to source domain. Meanwhile, a cycle consistency loss is also used to ensure that each unique image in the source domain can be transferred to a corresponding image in the target domain and reconstructed. The cycle consistency loss can be expressed as:

$$L_{cyc}\,(G_{S\rightarrow T},\, G_{T\rightarrow S}) = E_{X_S\sim P_{data}(X_S)}[\|X_{S\rightarrow T\rightarrow S} - X_S\|] + E_{X_T\sim P_{data}(X_T)}[\|X_{T\rightarrow S\rightarrow T} - X_T\|] \quad (3)$$

Where $X_{S\rightarrow T\rightarrow S}$ and $X_{T\rightarrow S\rightarrow}$T denote the reconstructed images of the source and target domains, where $X_{S\rightarrow T\rightarrow S} = G_{S\rightarrow T}(G_{T\rightarrow S}(X_S))$ and $X_{T\rightarrow S\rightarrow T} = G_{T\rightarrow S}(G_{S\rightarrow T}(X_T))$, respectively.

One potential concern associated with domain-transfer networks is the introduction of biases that may alter pore connectivity or interfacial geometry. In the present framework, this risk is mitigated by applying the segmented dry-state image as a structural mask to the enhanced datasets, thereby preserving the original pore-space topology and connectivity throughout the enhancement process. Nevertheless, domain-transfer approaches may still introduce subtle modifications to fluid-fluid interfaces or generate phase distributions resembling those observed in the target domain. Such effects are partially constrained by the cycle-consistency loss, which penalizes unrealistic mappings and encourages preservation of the underlying image content. An additional advantage of the proposed approach is that it does not require voxel-wise registration between low-quality and high-quality scans during training, reducing preprocessing requirements and avoiding errors associated with imperfect image alignment.

In terms of the training schedule, the network is trained using the Adam optimizer. The training starts with an initial learning rate of $1e^{-5}$ and a batch size of 16. The training spans 100 epochs, during which the learning rate is halved whenever the loss plateaus for 5 epochs. An overall of 10,000 training patches with a size of 96^2 pixels were collected for each stage.

3 Results

3.1 Image Quality Enhancement of Fast Micro-CT Scans

Figure 5 demonstrates the effect of the deep learning enhancement workflow on the ultrafast 1R dynamic micro-CT reconstruction. The high-quality dry scan provides a clear reference for the sandstone pore structure and solid matrix, while the raw 1R image shows the brine distribution during imbibition but with noticeably reduced image quality. This reduction in quality is expected because the 1R reconstruction was generated from limited number of projections to achieve a temporal resolution of approximately 2.8 s per 3D volume. As a result, the raw image contains substantial noise, reduced phase contrast, and less clearly defined boundaries between the brine phase, air-filled pore space, and solid grains.

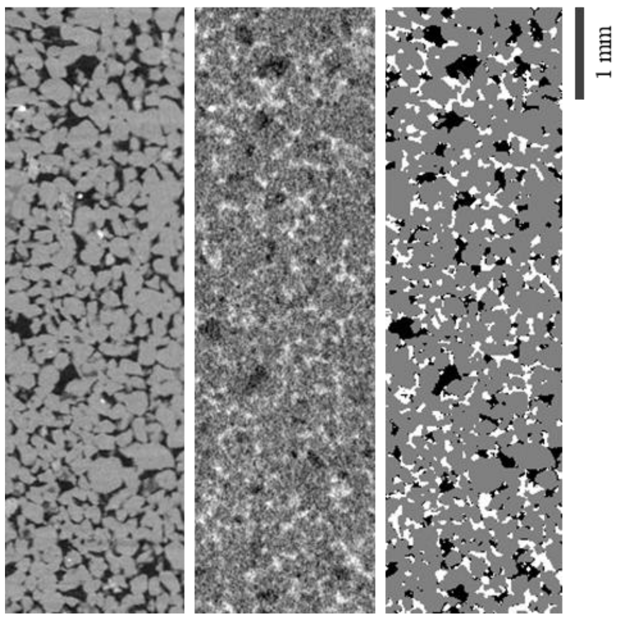

(a) (b) (c)

Fig. 5. Image quality enhancement using the deep learning workflow: (a) high-quality dry scan, (b) raw 1R dynamic scan acquired at 2.8 s temporal resolution, and (c) deep learning-enhanced 1R image.

The enhancement produces a clear visual improvement relative to the raw 1R reconstruction. After deep learning enhancement, the brine phase becomes more clearly resolved, and the pore boundaries appear sharper and more continuous. This improvement is required for subsequent quantitative analysis, including mass balance, pore-size distribution, morphological measurements, and saturation profiles.

The dry scan was acquired as a high-quality static reference (3 μm), while the dynamic 1R image was reconstructed at a voxel size of approximately 15 μm. The enhanced image was generated with an output voxel size of approximately 6.2 μm. The enhanced image therefore preserves the main advantage of the 1R acquisition, which is its high temporal resolution, while improving the image quality required for segmentation and interpretation.

The enhancement workflow was applied to the full dynamic dataset, allowing the time evolution of brine invasion to be analysed from sequential 1R volumes rather than from isolated static images. This preserves the temporal advantage of the ultrafast acquisition while improving the phase visibility needed for segmentation.

3.2 Effect of Temporal Resolution on Brine Dynamics

The effect of temporal resolution is shown more clearly in Figure 6, where equivalent stages of the experiment are compared using the 8R, 4R, and deep learning-enhanced 1R datasets. Since the acquisition time for a single rotation was approximately 2.8 s, the corresponding temporal windows for the 4R and 8R reconstructions are 11.2 s and 22.4 s, respectively.

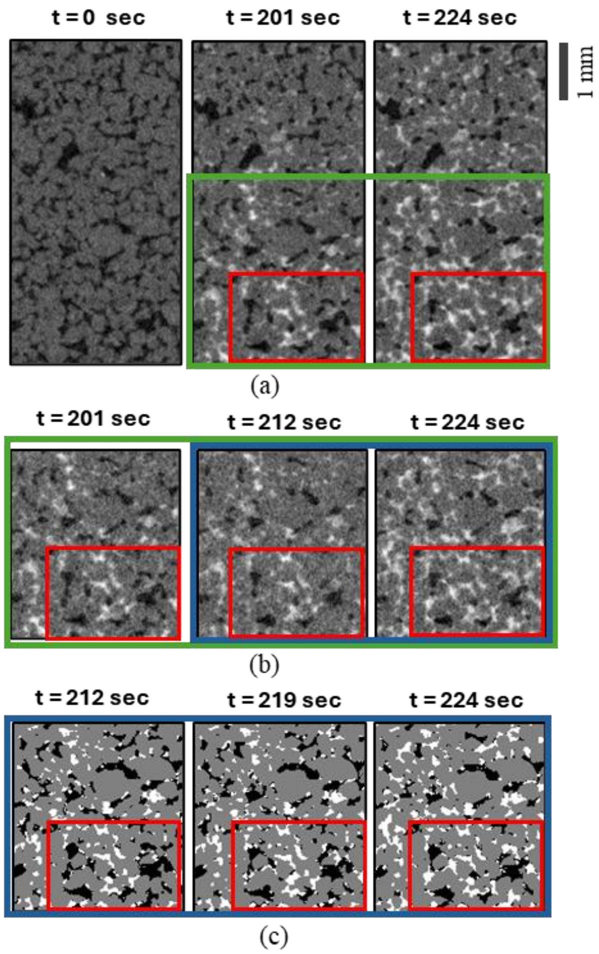

Fig. 6. Temporal resolution comparison between a) 8R, b) 4R, and c) deep learning-enhanced 1R reconstructions.

In the 8R dataset (Fig. 6a), three consecutive images corresponding to approximately 0 s (dry image), 201 s, and 224 s illustrate the overall advancement of the brine front. However, because each 8R image represents a 22.4 s temporal window, pore-scale displacement events occurring within this interval are temporally averaged, limiting the information available on intermediate invasion stages. The corresponding 4R reconstructions

(Fig. 6b) at approximately 201 s, 212 s, and 224 s provide an additional temporal state at 212 s that partially resolves the brine-front evolution not visible in the 8R images, although some temporal averaging remains due to the 11.2 s reconstruction window. The deep learning-enhanced 1R images (Fig. 6c) further refine the temporal sampling between 212 s and 224 s, capturing intermediate stages of brine movement that are absent in the 4R reconstructions. Consequently, the enhanced 1R sequence enables more continuous tracking of the displacement front and resolves transient pore-filling configurations that are obscured in the 4R and 8R datasets.

To quantify the image-quality trade-off associated with increasing temporal resolution, the peak signal-to-noise ratio (PSNR) was calculated using the 8R reconstruction as a reference:

$$PSNR = 10 \ \log_{10}\left(\frac{Imax^2}{MSE}\right), \quad (4)$$

where $Imax$ is the maximum possible image intensity and MSE is the mean squared error between the tested image and the reference image. The 4R image yielded a PSNR of 25.06 dB, whereas the raw 1R image produced a lower value of 18.19 dB, reflecting the expected reduction in grayscale fidelity associated with ultrafast acquisition. Since the 8R image is not a true ground-truth image, PSNR is used here only as a relative measure of similarity between reconstruction conditions.

To further evaluate the proposed enhancement framework, the enhanced images were compared with a Non-Local Means (NLM) filter and a single-stage P3T-Net trained to directly translate 1R images into the HQ domain. Figure 7a presents the no-reference image quality metrics: Perception-based Image Quality Evaluator (PIQE) and Naturalness Image Quality Evaluator (NIQE), while Figure 7b compares the normalized grayscale intensity distributions. Among the tested methods, the two-stage P3T-Net produced the lowest PIQE and NIQE values and exhibited a grayscale distribution that most closely matched the target domain. These results indicate that progressively reducing the domain gap through an intermediate 8R domain improves image restoration compared with conventional filtering and single-stage domain transfer.

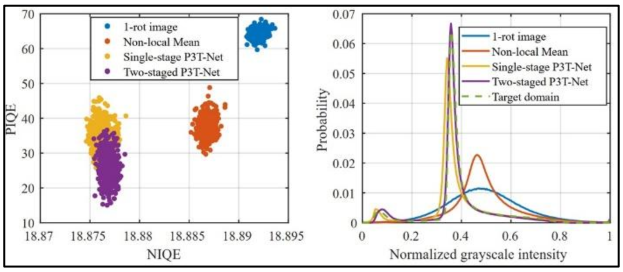

Fig. 7. Quantitative comparison of image enhancement approaches. (a) No-reference image quality assessment metrics, PIQE and NIQE. (b) Normalized grayscale intensity distributions for the corresponding images.

Overall, Figures 5-7 indicate that the enhanced 1R dataset provides the most suitable balance between temporal resolution and image quality for dynamic pore-scale analysis. While the 8R reconstructions offer higher visual quality, they are affected by temporal averaging. The enhanced 1R images retain the 2.8 s temporal resolution while providing sufficient phase contrast for segmentation and quantitative analysis. Therefore, the enhanced 1R dataset was selected for all subsequent analyses, whereas the 4R and 8R reconstructions were retained as reference cases.

3.3 Mass Balance Validation of Image-Derived Brine Volume

To validate the reliability of the segmented 1R images, a mass balance comparison was performed between the expected brine volume injected by the syringe pump and the brine volume measured directly from the segmented dynamic micro-CT images. This comparison provides an independent check on whether the enhanced and segmented 1R images capture the physically expected progression of brine imbibition.

The expected injected brine volume was calculated from the imposed flow rate:

$$V_{inj}\,(t) = Q \ x \ t \quad (5)$$

Where $V_{inj}\,(t)$ is the cumulative injected brine volume at time t, Q is the imposed injection flow rate, and t is time. In this experiment, brine was injected at a constant flow rate of 1.2 µL/min. Since the segmented images represent the reconstructed region of interest rather than the full core cross-section, the injected volume was corrected using the ratio between the imaged ROI cross-sectional area and the full core cross-sectional area for flow:

$$V_{inj}\,, ROI\ (t) = Q \ x \ t \ x \ \left[\frac{A_{ROI}}{A_{core}}\right] \quad (6)$$

where A_{ROI} is the cross-sectional area of the imaged region and A_{core} is the full cross-sectional area of the cylindrical core.

For the 5 mm diameter core, A_{core} = 19.63 mm². Based on the imaged ROI width of approximately 1.92 mm, A_{ROI} = 3.69 mm², giving an area correction factor of 0.188. Therefore, the corrected injection rate into the ROI was approximately:

$$Q_{ROI} = 1.2 \times 0.188 = 0.225\ \mu\text{L/min}$$

Thus, the expected injected brine volume within the imaged ROI was:

$$V_{inj}\,, ROI\ (t) = 0.225\text{t} \quad (7)$$

where t is in minutes and $V_{inj}\,, ROI$ is in µL.

The brine volume measured from the images was calculated from the segmented brine voxels:

$$V_{brine}\,, CT\ (t) = \ N_{brine}\ (t) \ x \ V_{voxel} \quad (8)$$

where $V_{brine}, CT\ (t)$ is the brine volume obtained from the segmented image at time t, $N_{brine}\ (t)$ is the number of voxels classified as brine, and V_{voxel} is the physical volume of one voxel. For the dynamic images, the voxel length was approximately 15 µm, giving a voxel volume of:

$$V_{voxel} = (0.015\text{ mm})^3 = 3.375 \times 10^{-6}\ \mu\text{L}.$$

As shown in Figure 8a, the expected cumulative brine volume calculated from the syringe-pump flow rate increases linearly with time, reflecting the constant injection rate imposed during the experiment. In contrast, the brine volume measured from the segmented dynamic micro-CT images follows a step-like trend, with periods of nearly constant volume interrupted by sudden increases. This difference is expected because the pump-derived curve represents the macroscopic injection input, whereas the image-derived curve reflects the local brine occupancy within the analysed region of interest (ROI), which occurs in pore-scale bursts as fluids rearrange under capillary-dominated conditions. Both curves show a comparable increasing trend up to approximately t = 9 min, indicating that the image-derived brine volume captures the early progression of brine invasion within the analysed ROI. After this point, ROI breakthrough (BT) is reached, and the segmented brine volume approaches a plateau. The syringe-pump-derived curve continues to increase because injection continues into the core, whereas the image-derived curve represents only the brine volume contained within the analysed ROI. Therefore, after ROI breakthrough, additional injected brine can continue to flow through already connected pathways and/or regions outside the analysed ROI without producing a proportional increase in the segmented brine volume.

The step-like behaviour of the image-derived brine volume is consistent with capillary-controlled displacement. Although brine is injected at a constant flow rate, the invading wetting phase does not advance continuously at the pore scale. Instead, imbibition proceeds through discrete pore-filling events, local meniscus rearrangements, and capillary-controlled redistribution. During the plateau regions of the curve, injected brine may be redistributed through already connected pathways, or the local capillary entry pressure required to invade additional pores within the ROI may not yet be reached. Once this threshold is reached, brine enters new pore space, producing a sudden increase in the segmented brine volume. This intermittent pore-scale response is also evident in Figure 8b, where the micro-CT image sequence shows a progressive increase in brine occupancy between sequential scans.

The agreement in the overall increasing trend supports the use of the segmented dynamic images for quantitative analysis, while the remaining differences between the two curves are expected. The ROI correction assumes uniform flow across the core cross-section, whereas brine invasion may be heterogeneous due to pore connectivity, local capillary-pressure variations, and preferential pathways. In addition, partial-volume effects at brine-air interfaces can influence voxel classification near the displacement front, and some injected brine may occupy connected pathways outside the analysed ROI. Therefore, the mass-balance comparison should be interpreted as a consistency check rather than an exact one-to-one volume match. The comparison confirms that the enhanced 1R images capture the expected progression of brine invasion and can be used for subsequent morphological and saturation-profile analysis.

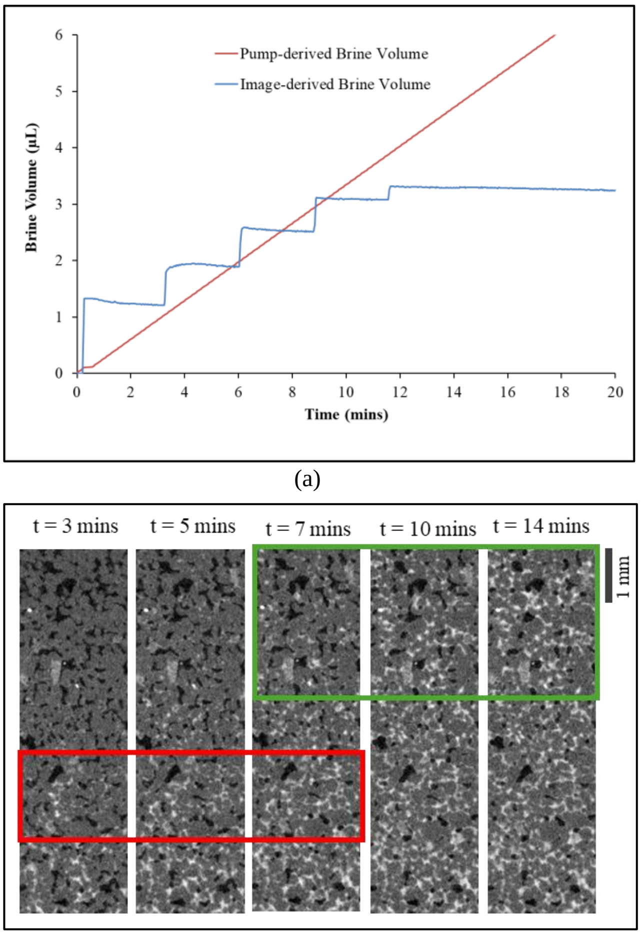

(a)

(b)

Fig. 8. a) Mass balance validation, b) visualisation of brine invasion in dynamic micro-CT images.

3.4 Pore-size-distribution validation of pore filling

The pore-size distribution (PSD) obtained from the dry reference image was compared with the PSD of the brine-occupied pore space at selected imbibition times to evaluate whether the segmented wet images captured physically consistent pore filling under water-wet conditions. The dry pore-space distribution represents the available pore volume in the Bentheimer sandstone before brine invasion, while the wet pore-space distributions indicate the subset of pores occupied by brine during the dynamic experiment.

As shown in Figure 9, the dry pore space exhibits a dominant peak at approximately 0.07 mm, with a secondary population around 0.09 mm and a low-frequency tail extending toward larger pore sizes. The brine-occupied pore-space distributions at 3, 5, 7, 10, and 14 min follow the same pore-size range and remain bounded by the dry PSD. This agreement is expected if the wet-phase segmentation is physically consistent, since brine should only occupy pore regions present in the dry reference image. Therefore, the fact that the wet curves fall within the dry pore-space envelope indicates that the segmentation and image-processing workflow do not generate artificial pore occupancy outside the resolved pore network.

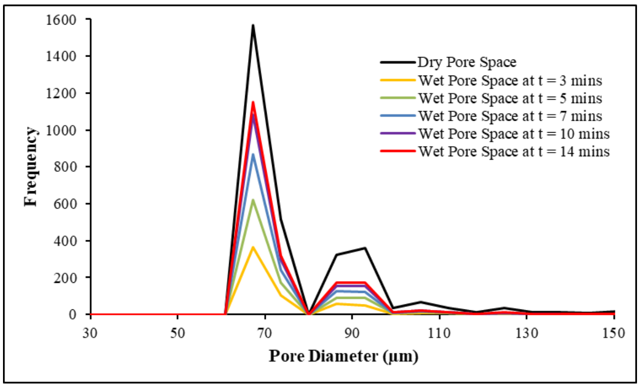

Fig. 9. Pore-size distribution comparison between the dry reference pore space and brine-occupied pore space during imbibition.

The temporal evolution of the wet pore-space distributions also reflects progressive brine invasion. At early time, the frequency of brine-occupied pores is relatively low, indicating limited pore filling near the beginning of imbibition. With increasing time, the wet PSD increases mainly within the dominant pore-size range of the dry image. This suggests that brine invasion occurs primarily through the main connected pore population rather than through unrealistic isolated features or noise-induced segmentation artifacts. The increase in wet pore frequency is especially clear around the principal pore-size mode, showing that the dynamic images capture the growth of brine occupancy within the dominant pore structure of the rock. The PSD evolution (Fig. 9) also indicates that smaller pore classes become more completely occupied by brine (pore diameter ~60-80 µm), whereas larger pore bodies (pore diameter ~80-100 µm) are less fully filled and may contain trapped non-wetting phase. This behaviour is physically consistent with imbibition under water-wet conditions, where the wetting phase preferentially invades smaller pores, throats, and connected wetting pathways, while non-wetting phase can remain trapped in larger pore bodies due to snap-off, bypassing, or capillary-controlled redistribution.

The PSD comparison provides an additional pore-scale consistency check by showing that the segmented brine volume is distributed within pore-size classes present in the dry reference image. This supports the interpretation that the enhanced dynamic images capture brine filling within the resolved pore network rather than producing artefacts outside the physically available pore space.

3.5 Morphological Evolution of Brine-Air Interfaces and Phase Connectivity

The segmented dynamic images were further analysed using morphological functions to quantify the evolution of brine-air interfacial area and fluid connectivity during imbibition. Water saturation was calculated from the segmented brine volume of the dynamic images. The brine-air interfacial area, A_{wn}, was then calculated to quantify the area of contact between the wetting brine phase and the non-wetting air phase. In this study, the interfacial area was evaluated as a function of water saturation and fitted using the following empirical model [51]:

$$a_{wn} = a_{crit} \frac{S_w(1-S_w)^n}{S_w + S_{scrit}(1-S_w)^m} \tag{9}$$

where a_{wn} is the brine-air specific interfacial area, a_{crit} is a scaling parameter controlling the maximum interfacial area, S_{scrit} controls the saturation at which the maximum interfacial area is reached, and m and n control the curvature of the left-hand and right-hand sides of the relationship, respectively. The fitted parameters used for the present dataset are 6 for a_{crit} , 0.1 for S_{scrit} , 1 for m, and 0.2 for n.

As shown in Figure 10a, the brine-air interfacial area varies systematically with water saturation. The fitted model follows the measured trend, indicating that the segmented images retain a consistent evolution of fluid-fluid interface area during imbibition. This suggests that the measured interfacial response is governed by displacement and redistribution of the phases rather than by random segmentation noise. This trend is also well aligned with similar studies in the literature [14,52,53].

The Euler characteristic was used as a topological descriptor of phase connectivity. In this analysis, the Euler characteristic was calculated for the air phase to assess the connectivity of the displaced non-wetting phase. In general, the Euler characteristic can be interpreted as:

$$\chi = \text{components} - \text{loops} + \text{cavities} \tag{10}$$

where χ is the Euler characteristic. A positive Euler characteristic generally indicates a structure dominated by disconnected components, whereas a negative Euler characteristic indicates a more connected structure with a greater number of loops or redundant pathways.

Figure 10b shows that the Euler characteristic of the non-wetting phase changes systematically with increasing water saturation. At lower saturation, the Euler characteristic is negative, indicating that the non-wetting phase has a connected, loop-rich topology. This suggests that, during the early stage of imbibition, the fluid configuration contains connected pathways and complex pore-scale connectivity rather than isolated disconnected clusters. As water saturation increases, the Euler characteristic increases and eventually becomes positive. This transition indicates a shift in topology from a connected structure dominated by loops to a structure increasingly dominated by disconnected components. This change is consistent with the expected evolution the displaced air phase during imbibition. As brine invades the pore space, the air phase is progressively displaced and broken into smaller disconnected regions. The fragmentation of the non-wetting phase increases the number of isolated components, which drives the Euler characteristic toward positive values. Therefore, the transition from negative to positive Euler characteristic reflects a change in phase connectivity associated with displacement, fragmentation, and trapping of the non-wetting phase. Additionally, the linear trend of increasing Euler Characteristics of the non-wetting phase during imbibition is consistent with previous experimental studies [14,52,53].

Together, the interfacial area and Euler characteristic show that the enhanced 1R dataset preserves quantitative information beyond phase volume alone. The interfacial-area trend captures the evolution of brine–air contact during imbibition, while the Euler characteristic reflects changes in non-wetting phase connectivity and fragmentation. These descriptors support the use of the enhanced dynamic images for pore-scale morphological analysis.

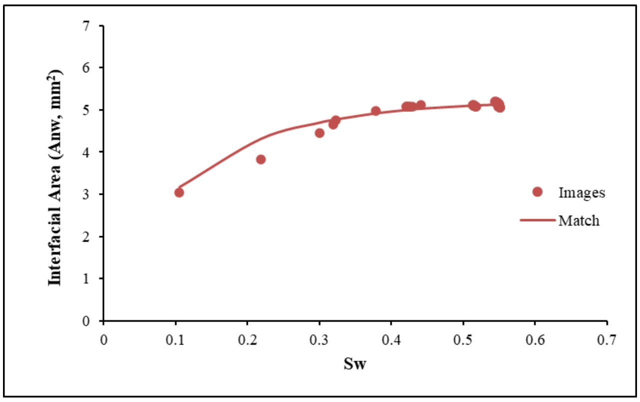

(a)

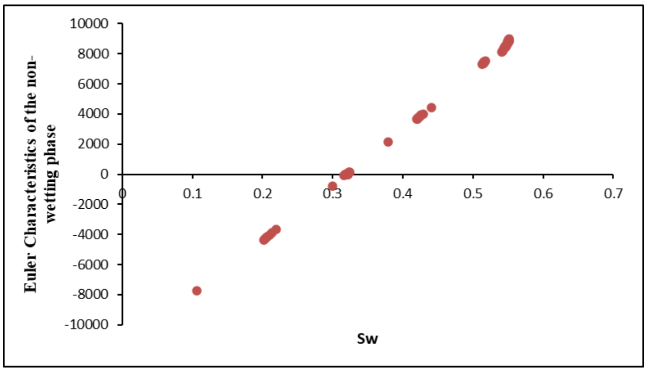

(b)

Figure 10. a) Brine-air interfacial area as a function of water saturation and b) Euler characteristic.

3.6 Saturation Profiles During Brine Imbibition

To further investigate the spatial evolution of brine imbibition, one-dimensional saturation profiles were extracted from the segmented dynamic images along the core axis. The saturation profile provides information on how brine is distributed within the pore space at each time step.

As shown in Figure 11, the saturation profiles show a clear progression of the brine phase along the core with time. At early times, the brine saturation is high only near the inlet, while the upper part of the core remains mostly air-filled. As imbibition proceeds, the saturation front progressively shifts toward larger values of x/L, confirming upward movement of the wetting phase through the pore network. The profiles also show that the brine saturation is generally highest near the inlet and decreases toward the outlet, which is consistent with bottom-up injection.

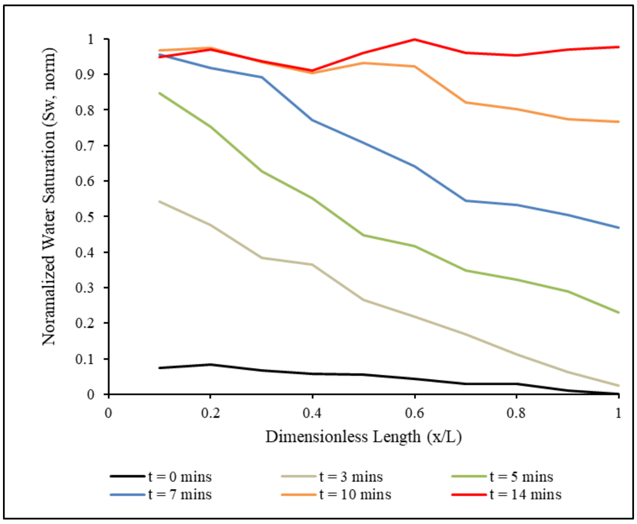

Figure 11. Normalized water saturation profiles during brine imbibition before breakthrough.

The displacement does not appear as a sharp piston-like front. Instead, the transition from high saturation to low saturation occurs over a finite distance, indicating that the brine front is spatially distributed. This spreading is expected in sandstone because the pore space is heterogeneous and the invading brine does not fill all pores at the same axial position simultaneously. Local invasion is controlled by pore-throat geometry, capillary entry pressure, and connectivity for the small ROI that is imaged. As a result, some pores ahead of the average front may be invaded earlier through preferential pathways, while some pores behind the front may remain only partially filled or air-occupied due to bypassing or local trapping.

The broad transition zone indicates capillary dispersion during imbibition for the entire imaged ROI. Rather than advancing as a uniform plug, the brine front spreads because local invasion is controlled by pore-throat geometry, capillary thresholds, and connectivity. This is consistent with the step-like volume response observed in the mass-balance analysis and further indicates that the displacement is governed by local pore-scale events.

3.7 Computational Efficiency of the Deep Learning Workflow

The computational cost of the enhancement workflow was evaluated to determine whether the method can be applied to full 4D micro-CT datasets. This is necessary because dynamic imaging produces hundreds of sequential 3D volumes, and the enhancement step must remain practical for post-processing rather than only for selected images.

The computational time was measured using an NVIDIA RTX 4090 GPU, and the results are summarized in Table 1. Training the full cascading denoising workflow, which maps the 1R domain toward the high-quality domain, required approximately 4 h. This training step represents the most computationally expensive part of the workflow; however, it is performed only once. After training, the model can be applied directly to newly reconstructed 1R images with substantially shorter processing times.

Table 1. Computational time required for the cascading deep learning enhancement workflow.

Processing step	Input → Output domain	Time required
Model training	Cascading denoising from 1R to HQ Domain	4 hours
Denoising stage 1	1R → 8R	2 seconds
Denoising stage 2	8R → high-quality	4 seconds
Total Denoising	1R → high-quality	6 seconds
Full 4D dataset enhancement	428 raw 1R images	42 minutes

For a single 3D image (128x128x437 voxels), the first denoising stage, which maps the 1R reconstruction to the 8R domain, required approximately 2 s. The second denoising stage, which maps the 8R output to the high-quality domain, required approximately 4 s. Therefore, the total inference time required to enhance one 1R 3D image through the full cascading workflow was approximately 6 s. When applied to the complete dynamic dataset, consisting of 428 raw 1R images, the trained model required approximately 42 min to enhance all time steps. These timings show that the workflow is feasible for post-processing large dynamic datasets. Although training requires several hours, it is performed once for the image domains considered here. After training, inference is rapid enough to enhance hundreds of 1R volumes within less than one hour, making the approach suitable for routine analysis of ultrafast laboratory-based 4D micro-CT data.

4 Conclusions

This study demonstrates a deep learning-assisted benchtop micro-CT workflow for second-scale 4D imaging of brine imbibition in Bentheimer sandstone. By combining ultrafast 1R acquisition with cascading P3T-Net enhancement, dynamic volumes were reconstructed at approximately 2.8 s temporal resolution while retaining sufficient image quality for phase segmentation and quantitative pore-scale analysis.

The enhanced 1R images showed improved brine–air–solid phase separation compared with the raw 1R reconstructions. Mass-balance comparison showed that the image-derived brine volume followed the expected increasing trend, while its step-like evolution reflected intermittent pore-scale filling and capillary-controlled redistribution.

Morphological analysis showed that the enhanced images retained information on both interfacial structure and phase connectivity, that was consistent with trends reported in the literature. The brine-air interfacial area varied consistently with water saturation, and the Euler characteristic captured the transition in phase topology associated with displacement and fragmentation of the non-wetting phase.

Saturation profiles revealed a distributed capillary dominated transition zone rather than a sharp piston-like front, indicating front spreading caused by pore-scale heterogeneity, local capillary thresholds, and non-uniform pore filling. This highlights the value of second-scale imaging for resolving the evolving structure of the displacement front.

The computational performance of the workflow also supports its practical application to large 4D datasets. The cascading model required approximately 4 h for training on an RTX 4090 GPU, after which inference required approximately 6 s per 3D image. The complete dynamic dataset was enhanced in approximately 42 min, demonstrating that the method is computationally feasible for routine post-processing of time-resolved micro-CT experiments.

It is worth noting that despite the substantial improvement in temporal resolution achieved by the proposed workflow, some limitations remain. The 2.8 s temporal resolution captures the progression of fluid displacement but may not fully resolve the fastest pore-scale events, such as Haines jumps, snap-off events, and rapid interfacial rearrangements that can occur on millisecond timescales. In addition, partial volume effects at fluid interfaces remain a source of uncertainty because voxels located at phase boundaries may contain mixed-phase information, potentially affecting saturation estimates, interfacial area calculations, and mass-balance analyses. Future work will focus on combining the proposed framework with synchrotron-based imaging systems, combining the approaches has the potential to reach sub-second temporal resolution. Furthermore, developing super-resolution image enhancement approaches to improve the representation of fluid interfaces and further increase the accuracy of pore-scale flow characterization would be important future work.

Overall, the results show that deep learning-enhanced ultrafast benchtop micro-CT can provide quantitative time-resolved measurements of brine imbibition, including mass balance, pore-size distribution, interfacial area, Euler characteristic, and saturation profiles. The workflow offers an accessible platform for studying transient multiphase flow processes relevant to CO_2 storage, underground hydrogen storage, and groundwater flow. Future work should extend the approach to different rock types, wettability conditions, and flow regimes, and should further validate the enhanced images against independent experimental or numerical benchmarks.

References

1. S. Krevor, M.J. Blunt, S.M. Benson, C.H. Pentland, C. Reynolds, A. Al-Menhali, et al., Capillary trapping for geologic carbon dioxide storage: From pore-scale physics to field-scale implications, Int. J. Greenh. Gas Control **40**, 221–237 (2015)
2. M.J. Blunt, Multiphase Flow in Permeable Media: A Pore-Scale Perspective (Cambridge University Press, Cambridge, 2017)
3. T. Pak, L.F. de L. Luz Jr., T. Tosco, G.S.R. Costa, P.R.R. Rosa, N.L. Archilha, Pore-scale investigation of the use of reactive nanoparticles for in situ remediation of contaminated groundwater source, Proc. Natl. Acad. Sci. U.S.A. **117**, 13366–13373 (2020)
4. W. Goethals, T. Bultreys, Z. Manigrasso, A. Mascini, J. Aelterman, M.N. Boone, Dynamic CT reconstruction with improved temporal resolution for scanning of fluid flow in porous media, Water Resour. Res. **58**, e2021WR031365 (2022)
5. S. Berg, H. Ott, S.A. Klapp, A. Schwing, R. Neiteler, N. Brussee, et al., Real-time 3D imaging of Haines jumps in porous media flow, Proc. Natl. Acad. Sci. U.S.A. **110**, 3755–3759 (2013)
6. S. Pavuluri, J. Maes, J. Yang, M. Regaieg, A. Moncorgé, F. Doster, Towards pore network modelling of spontaneous imbibition: Contact angle dependent invasion patterns and the occurrence of dynamic capillary barriers, Comput. Geosci. **24**, 951–969 (2020)
7. I. Zacharoudiou, E.M. Chapman, E.S. Boek, J.P. Crawshaw, Pore-filling events in single junction micromodels with corresponding lattice Boltzmann simulations, J. Fluid Mech. **824**, 550–573 (2017)
8. R. Hu, J. Wan, Z. Yang, Y.-F. Chen, T. Tokunaga, Wettability and flow rate impacts on immiscible displacement: A theoretical model, Geophys. Res. Lett. **45**, 3077–3086 (2018)
9. R. Lenormand, C. Zarcone, A. Sarr, Mechanisms of the displacement of one fluid by another in a network of capillary ducts, J. Fluid Mech. **135**, 337–353 (1983)
10. W.B. Haines, Studies in the physical properties of soil. V. The hysteresis effect in capillary properties, and the modes of moisture distribution associated therewith, J. Agric. Sci. **20**, 97–116 (1930)
11. K. Singh, H. Menke, M. Andrew, Q. Lin, C. Rau, M.J. Blunt, et al., Dynamics of snap-off and pore-filling events during two-phase fluid flow in permeable media, Sci. Rep. **7**, 5192 (2017)
12. C.A. Reynolds, H. Menke, M. Andrew, M.J. Blunt, S. Krevor, Dynamic fluid connectivity during steady-state multiphase flow in a sandstone, Proc. Natl. Acad. Sci. U.S.A. **114**, 8187–8192 (2017)
13. R.T. Armstrong, A. Georgiadis, H. Ott, D. Klemin, S. Berg, Critical capillary number: Desaturation studied with fast X-ray computed microtomography, Geophys. Res. Lett. **41**, 55–60 (2014)
14. S. Schlüter, S. Berg, M. Rücker, R.T. Armstrong, H.J. Vogel, R. Hilfer, et al., Pore-scale displacement mechanisms as a source of hysteresis for two-phase flow in porous media, Water Resour. Res. **52**, 2194–2205 (2016)
15. S. Schlüter, S. Berg, T. Li, H.-J. Vogel, D. Wildenschild, Time scales of relaxation dynamics during transient conditions in two-phase flow, Water Resour. Res. **53**, 4709–4724 (2017)
16. T. Bultreys, M.A. Boone, M.N. Boone, T. De Schryver, B. Masschaele, L. Van Hoorebeke, et al., Fast laboratory-based micro-computed tomography for pore-scale research: Illustrative experiments and perspectives on the future, Adv. Water Resour. **95**, 341–351 (2016)
17. D. Wildenschild, A.P. Sheppard, X-ray imaging and analysis techniques for quantifying pore-scale structure and processes in subsurface porous medium systems, Adv. Water Resour. **51**, 217–246 (2013)
18. V. Cnudde, M.N. Boone, High-resolution X-ray computed tomography in geosciences: A review of the current technology and applications, Earth Sci. Rev. **123**, 1–17 (2013)
19. Y. Niu, Y. Da Wang, P. Mostaghimi, J.E. McClure, J. Yin, R.T. Armstrong, Geometrical-based generative adversarial network to enhance digital rock image quality, Phys. Rev. Appl. **15**, 064033 (2021)
20. K.R. Tekseth, D.W. Breiby, 4D imaging of two-phase flow in porous media using laboratory-based micro-computed tomography, Water Resour. Res. **60**, e2023WR036514 (2024)
21. D.E. Meisenheimer, M.L. Rivers, D. Wildenschild, Optimizing pink-beam fast X-ray microtomography for multiphase flow in 3D porous media, J. Microsc. **277**, 100–106 (2020)
22. F. García-Moreno, P.H. Kamm, T.R. Neu, F. Bülk, M.A. Noack, M. Wegener, et al., Tomoscopy: Time-resolved tomography for dynamic processes in materials, Adv. Mater. **33**, 2104659 (2021)
23. R. Mokso, C.M. Schlepütz, G. Theidel, H. Billich, E. Schmid, T. Celcer, et al., GigaFRoST: The gigabit fast readout system for tomography, J. Synchrotron Radiat. **24**, 1250–1259 (2017)
24. E.A. Chavez Panduro, B. Cordonnier, K. Gawel, I. Børve, J. Iyer, S.A. Carroll, et al., Real-time 3D observations of Portland cement carbonation at CO_2 storage conditions, Environ. Sci. Technol. **54**, 8323–8332 (2020)
25. A. Piovesan, T. Van De Looverbosch, P. Verboven, C. Achille, C.P. Cabrera, E. Boller, et al., 4D synchrotron microtomography and pore-network modelling for direct in situ capillary flow visualization in 3D printed microfluidic channels, Lab Chip **20**, 2403–2411 (2020)
26. M. Rücker, S. Berg, R. Armstrong, A. Georgiadis, H. Ott, L. Simon, et al., The fate of oil clusters during fractional flow: Trajectories in the saturation-capillary number space, Int. Symp. Soc. Core Anal. (2015)

27. M. Rücker, S. Berg, R.T. Armstrong, A. Georgiadis, H. Ott, A. Schwing, et al., From connected pathway flow to ganglion dynamics, Geophys. Res. Lett. **42**, 3888–3894 (2015)
28. S. Berg, R. Armstrong, H. Ott, A. Georgiadis, S.A. Klapp, A. Schwing, et al., Multiphase flow in porous rock imaged under dynamic flow conditions with fast X-ray computed microtomography, Petrophysics **55**, 304–312 (2014)
29. S. Youssef, H. Deschamps, J. Dautriat, E. Rosenberg, R. Oughanem, E. Maire, et al., 4D imaging of fluid flow dynamics in natural porous media with ultra-fast X-ray microtomography, Int. Symp. Soc. Core Anal., 1–12 (2013)
30. L. Leu, S. Berg, F. Enzmann, R.T. Armstrong, M. Kersten, Fast X-ray micro-tomography of multiphase flow in Berea sandstone: A sensitivity study on image processing, Transp. Porous Media **105**, 451–469 (2014)
31. M. Andrew, H. Menke, M.J. Blunt, B. Bijeljic, The imaging of dynamic multiphase fluid flow using synchrotron-based X-ray microtomography at reservoir conditions, Transp. Porous Media **110**, 1–24 (2015)
32. T. Bultreys, K. Singh, A.Q. Raeini, L.C. Ruspini, P.-E. Øren, S. Berg, et al., Verifying pore network models of imbibition in rocks using time-resolved synchrotron imaging, Water Resour. Res. **56**, e2019WR026587 (2020)
33. T. Bultreys, S. Ellman, C.M. Schlepütz, M.N. Boone, G.K. Pakkaner, S. Wang, et al., 4D microvelocimetry reveals multiphase flow field perturbations in porous media, Proc. Natl. Acad. Sci. U.S.A. **121**, e2316723121 (2024)
34. G.-H. Chen, J. Tang, S. Leng, Prior image constrained compressed sensing: A method to accurately reconstruct dynamic CT images from highly undersampled projection data sets, Med. Phys. **35**, 660–663 (2008)
35. G.R. Myers, A.M. Kingston, T.K. Varslot, M.L. Turner, A.P. Sheppard, Dynamic tomography with a priori information, Appl. Opt. **50**, 3685–3690 (2011)
36. G. Van Eyndhoven, K.J. Batenburg, D. Kazantsev, V. Van Nieuwenhove, P.D. Lee, K.J. Dobson, et al., An iterative CT reconstruction algorithm for fast fluid flow imaging, IEEE Trans. Image Process. **24**, 4446–4458 (2015)
37. S.A. Mäkiharju, J. Dewanckele, M. Boone, C. Wagner, A. Griesser, Tomographic X-ray particle tracking velocimetry: Proof-of-concept in a creeping flow, Exp. Fluids **63**, 16 (2022)
38. W. Goethals, T. Bultreys, S. Berg, M.N. Boone, J. Aelterman, Dyrect computed tomography: Dynamic reconstruction of events on a continuous timescale, IEEE Trans. Comput. Imaging (2025)
39. M. Heyndrickx, T. Bultreys, W. Goethals, L. Van Hoorebeke, M.N. Boone, Improving image quality in fast, time-resolved micro-CT by weighted back projection, Sci. Rep. **10**, 18029 (2020)
40. I. Goodfellow, J. Pouget-Abadie, M. Mirza, B. Xu, D. Warde-Farley, S. Ozair, et al., Generative adversarial nets, Adv. Neural Inf. Process. Syst. **27** (2014)
41. Q. Yang, P. Yan, Y. Zhang, H. Yu, Y. Shi, X. Mou, et al., Low-dose CT image denoising using a generative adversarial network with Wasserstein distance and perceptual loss, IEEE Trans. Med. Imaging **37**, 1348–1357 (2018)
42. H.S. Park, J. Baek, S.K. You, J.K. Choi, J.K. Seo, Unpaired image denoising using a generative adversarial network in X-ray CT, IEEE Access **7**, 110414–110425 (2019)
43. J. Xie, L. Xu, E. Chen, Image denoising and inpainting with deep neural networks, Adv. Neural Inf. Process. Syst. **25** (2012)
44. K. Zhang, W. Zuo, Y. Chen, D. Meng, L. Zhang, Beyond a Gaussian denoiser: Residual learning of deep CNN for image denoising, IEEE Trans. Image Process. **26**, 3142–3155 (2017)
45. V. Jain, S. Seung, Natural image denoising with convolutional networks, Adv. Neural Inf. Process. Syst. **21** (2008)
46. J. Ho, A. Jain, P. Abbeel, Denoising diffusion probabilistic models, Adv. Neural Inf. Process. Syst. **33**, 6840–6851 (2020)
47. E.S. Mathew, S.J. Jackson, D. Wildenschild, P. Mostaghimi, K. Tang, R.T. Armstrong, Deep learning assisted denoising of fast polychromatic X-ray micro-CT imaging of multiphase flow in porous media, Comput. Geosci. **204**, 105990 (2025)
48. H. Friis, H. Nese, G. Luani, C. Pryme, L. Rennan, B. Chattopadhyay, et al., Implicit neural representation for fast 4D computed tomography of multiphase flow in porous media, Commun. Phys. **8**, 339 (2025)
49. M. Bizhani, O.H. Ardakani, E. Little, Reconstructing high fidelity digital rock images using deep convolutional neural networks, Sci. Rep. **12**, 4264 (2022)
50. K. Tang, R.T. Armstrong, P. Mostaghimi, Y. Niu, Q. Meyer, C. Zhao, et al., Scaling deep learning for material imaging with a pseudo 3D model for domain transfer, Nat. Commun. **16**, 11293 (2025)
51. D.E. Meisenheimer, D. Wildenschild, Predicting the effect of relaxation on interfacial area development in multiphase flow, Water Resour. Res. **57**, e2020WR028770 (2021)
52. A. Adila, M. Ebadi, W. Xi, X. Qi, Y. Jing, P. Mostaghimi, et al., Comparison of relative permeability hysteresis in oil-brine and gas-brine systems: A pore-scale investigation, Int. J. Multiph. Flow **194**, 105483 (2026)
53. M. Ebadi, D. Meisenheimer, D. Wildenschild, J. McClure, P. Mostaghimi, R.T. Armstrong, Topological evolution: An unexplored aspect of hysteresis for multiphase flow in porous media, Phys. Fluids **38** (2026)